In situ formation of ionically conductive nanointerphase on Si particles for stable battery anode

Xiaoxue Chen[1], Gaofeng Ge[1], Wenyu Wang[1], Bao Zhang[2], Jianjun Jiang[2], Xuelin Yang[3], Yuzhang Li[4], Li Wang[5*], Xiangming He[5] & Yongming Sun[1*]

[1]*Wuhan National Laboratory for Optoelectronics, Huazhong University of Science and Technology, Wuhan 430074, China;*
[2]*School of Optical and Electronic Information, Huazhong University of Science and Technology, Wuhan 430074, China;*
[3]*College of Electrical Engineering & New Energy, Hubei Provincial Collaborative Innovation Center for New Energy Microgrid, China Three Gorges University, Yichang 443002, China;*
[4]*College of Materials and Chemical Engineering, University of California, Los Angeles 90095, USA;*
[5]*Institute of Nuclear and New Energy Technology, Tsinghua University, Beijing 100084, China*

Silicon (Si) is a promising anode candidate for next-generation lithium-ion batteries (LIBs) due to its high theoretical capacity. Solar Si photovoltaic waste possesses good purity and high output. Using it as the raw material for battery anodes can synchronously solve the problem of solid waste pollution and enable high energy density LIBs. A critical issue impeding the practical application of Si is the undesirable side reactions at the electrolyte-particle interface and the resulting increase in impedance during cycling. Herein, a Si–P core shell structure with chemical bonding at the Si–P interface is fabricated through a simple mechanical alloying reaction between red P and solar Si photovoltaic waste. The P nanoshell with thickness within 15 nm converts to Li_3P during the initial lithiation process and maintains its phase on cycling. The as-formed Li_3P nanolayer functions as a stable, ionically conductive protective layer that reduces the direct contact between Si and electrolytes, and thus suppresses undesired side reactions. The Si–P nanocomposite exhibits stable electrochemical cycling with a high reversible capacity of 1,178 mAh g^{-1} after 500 cycles at 1,200 mA g^{-1}, as well as excellent rate capability (912 mAh g^{-1} at 2 C). With 15 wt% addition to graphite, a graphite/Si–P hybrid electrode shows a high overall reversible specific capacity of 447 mAh g^{-1} and 88.3% capacity retention after 100 cycles at high areal capacity of 2.64 mAh cm^{-2} at 100 mA g^{-1}, indicating its promise as a drop-in anode in practical LIBs.

silicon anode, Li_3P, interface, stability, lithium-ion batteries

1 Introduction

Lithium-ion batteries (LIBs) are the dominating power source for portable electronics and are penetrating into the electric vehicles market [1–5]. However, the energy density of current LIBs based on the traditional intercalation cathode (*i.e.* $LiCoO_2$ and $LiFePO_4$) and anode (*i.e.* graphite) is approaching the theoretical limit, which cannot meet the increasing requirement for various applications [5,6]. With similar working potential and over 10 times higher theoretical capacity than that of graphite (4,200 mAh g^{-1} for Si based on its full lithiation product of $Li_{4.4}Si$ and 372 mAh g^{-1} for graphite), Si possesses great opportunity to enable higher energy density of LIBs if the traditional graphite was replaced with Si-based materials [7–9]. During the initial

---

*Corresponding authors (email: wang-l@tsinghua.edu.cn, yongmingsun@hust.edu.cn)

charge process, electrochemical reduction of liquid electrolytes takes place, producing an ionically conductive yet electronically insulating passivating layer, namely solid-electrolyte interphase (SEI), on the anode surface. The SEI layer on a graphite anode is ultrathin (*i.e.* ~10 nm) and remains stable after the formation cycle, which enables stable electrochemical cycling with high Coulombic efficiency [10]. However, the situation for Si anodes is quite different. New Si surfaces are continuously exposed to electrolytes due to the large volumetric expansion and shrinkage of Si-based materials (~400%) during each lithiation/delithiation cycle, resulting in undesired side reactions with liquid electrolytes. Such processes cause the continuous growth of SEI upon cycling, accompanied with consumption of liquid electrolytes and active lithium, ever-increasing impedance for lithium-ion diffusion, and rapid degradation of electrochemical performances [11–13]. The instability of the electrode/electrolyte interface and electrolyte degradation would also lead to the evolution of gas, which aggravates the electrochemical performances [14,15].

To address the above issues, various strategies have been explored in the past 10 years with a focus on engineering the composition and structure of Si-based materials [16–19]. Important strategies, including the use of SiO_x to replace pure Si [20,21], carbon-coated Si nanoparticles [22,23], Si–C yolk-shell structure [24,25], Si–C pomegranate structure [26], Si-carbon watermelon structure [27], and conformal graphite/Si composite [28,29], have been shown to improve electrochemical performances due to the increased electronic conductivity, buffer effect for the volume change and/or suppressed side-reactions between liquid electrolytes and active Si. Moreover, engineering the electrolyte chemistry has also been successful in stabilizing the electrolyte-electrode interphase and improving the cycling stability of Si-based anodes [30,31]. Despite these advances, there still remains significant challenges in realizing a Si-based anode that meets commercial application's requirements, such as easy fabrication, low cost, and long lifespan. As a compromise between energy density and cycle life, the graphite/Si hybrid electrode has been considered for practical application in the near term (~5 years). The Si content in state-of-the-art graphite/Si hybrid is usually less than 5 wt% with the overall capacity of 400–450 mAh g^{-1} for the composite. Despite the increased capacity over pure graphite, the cycle life of the graphite/Si hybrid electrode is very limited in comparison to pure graphite (*i.e.* <300 cycles with 70% capacity retention), demonstrating the great challenges of using Si in large amounts with graphite.

Solar Si photovoltaics dominates the clean energy transition, which generates Si sawdust waste during the fabrication. The amount of produced Si waste increased year-by-year and reached ~1.62×10^5 tons in 2017 [32]. It is highly desirable to utilize such Si waste to fabricate high-capacity Si anodes for high-energy-density LIBs, which can not only achieve economic benefits, but also address the problem of Si solid waste. Herein, we report the construction of an ionically conductive Li_3P [33,34] nanolayer (within 15 nm) on Si waste particles to form Si–Li_3P core shell structures by a simple chemomechanical reaction between Si and red P, followed by the *in-situ* irreversible electrochemical alloy reaction of red P into Li_3P during the initial charge/discharge cycle. The main working potential of Si anodes locates at ~0.4 V, and the cutoff potential range for Si anodes is often in the range of 0.01–1 V (*vs.* Li^+/Li). During the initial lithiation process, the as-achieved Si–P core shell structure transforms into $Li_{4.4}Si$–Li_3P core shell structure in consideration of the full lithiation of Si and P (P + 3Li^+ + 3e^- → Li_3P, Si + 4.4Li^+ + 4.4e^- → $Li_{4.4}Si$, Figure 1a, b). During the delithiation process, lithium in $Li_{4.4}Si$ is reversibly extracted in the cutoff potential range below 1 V (*vs.* Li^+/Li), while Li_3P remains stable due to its higher delithiation potential above 1 V (*vs.* Li^+/Li, Figure 1a, b). Therefore, a stable Si (Li_xSi_y)–Li_3P core shell structure is maintained during the electrochemical charge/discharge cycling after the 1st lithiation cycle (Figure 1c). The improvement in rate capability and cycle performance of the as-achieved Si–P anode can be expected from two features of the composite. The Li_3P nanoshell provides high ionic conductivity (10^{-3} S cm^{-1}) [35,36] and reduces the direct contact between active Si and electrolytes, which enables enhanced lithium diffusion at the interface and suppresses the side reactions between the electrode and electrolyte. As a result, a high reversible capacity of 1,178 mAh g^{-1} was achieved for the Si–P composite after 500 cycles at the current density of 1,200 mA g^{-1}. Moreover, the Si–Li_3P electrode also displayed much better rate capability than pristine Si electrode. It delivered a high capacity of 912 mAh g^{-1} at 2 C. By contrast, the pristine Si electrode almost lost all its capacity (only 14 mAh g^{-1}) at this high rate. With the addition of 15 wt% Si–P into a commercial graphite electrode, the hybrid electrode showed high capacity retention of 88.3% after 100 cycles at 100 mA g^{-1} under a high areal capacity of 2.64 mAh cm^{-2}, showing promise for the practical application.

2   Experimental

2.1   Material preparation

In this work, Si photovoltaic waste from Golden Concord Holdings Limited was employed as the Si source, which was used as received without any treatment. Silicon solar-cell-waste and red P were used as starting materials for the fabrication of Si–P composite. The silicon solar-cell-waste powder was firstly ball-milled at 200 rpm to produce Si particles with the size range of 200–800 nm. Commercial red P powder and the as-produced Si powder were mixed with
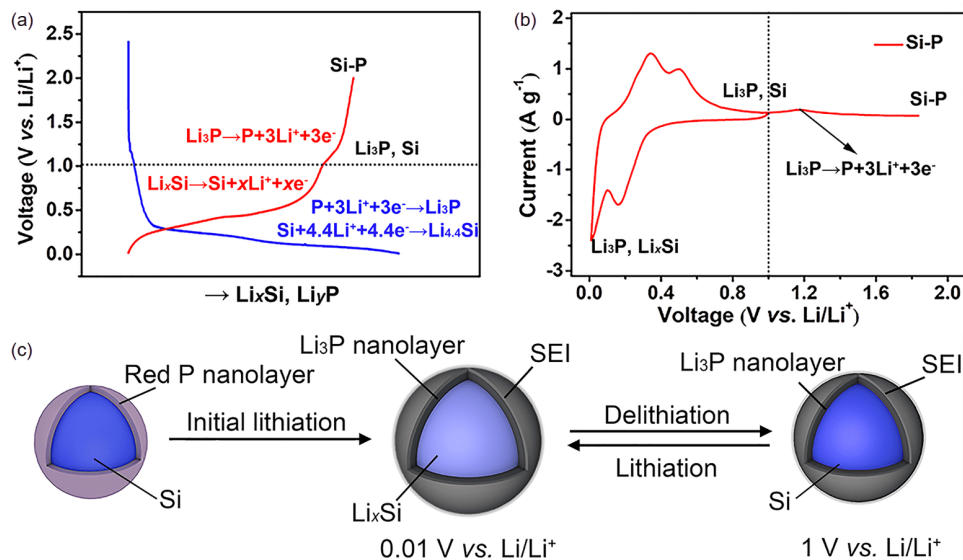
Figure 1 Electrochemical cycling of Si–P core-shell composite. (a) The first-cycle voltage-lithiation degree plot and (b) cyclic voltammograms (CVs) of Si–P electrode at 0.1 mV s^{-1}. (c) Schematic of a Si–P core-shell structured particle during the lithiation/delithiation cycling in the cutoff potential range of 0.01–1 V (*vs.* Li/Li$^+$). During the initial lithiation process, P irreversibly converts to Li$_3$P and Li in Li$_3$P will not be extracted below 1 V (*vs.* Li/Li$^+$). A stable Si(Li$_x$Si$_y$)–Li$_3$P core-shell structure is formed during the following electrochemical cycling in the cutoff potential range of 0.01–1 V (*vs.* Li/Li$^+$) (color online).

Si/P weight ratio of 5/1 and then ball-milled at 350 rpm for 6 h in the Ar atmosphere to fabricate Si–P composite.

2.2   Material characterizations

X-ray diffraction (XRD) information was collected using a PANalytical B. V. instrument with Cu $K_{\alpha 1}$ radiation operated at an accelerating voltage of 40 kV and current of 40 mA. X-ray photoelectron spectroscopy (XPS) measurement was carried out on a VG MultiLab 2000 system with a monochromatic Al K_α X-ray source. The morphology and the structure of the electrode and materials were characterized by scanning electron microscopy (SEM) with an energy spectrometer of Nova NanoSEM 450 and transmission electron microscopy (TEM, FEI Talos f200x). Before characterization analysis of the cycled electrodes, coin-type cells were disassembled, and the cycled electrodes were taken out and washed with 1,3-dioxolane (DOL) in an Ar filled glovebox. The electrode was used for *ex-situ* SEM analysis after the volatilization of the solvent. The powder was scraped from the dried electrodes, dispersed in DOL and loaded onto a copper grid for sample fabrication for the *ex-situ* TEM analysis.

2.3   Electrochemical characterizations

Slurry for Si–P electrodes and pristine Si electrodes was fabricated by mixing active materials (70 wt%), carbon black (20 wt%) and carboxymethyl cellulose (CMC) binder (10 wt%) in water, and then it was coated onto a copper foil and dried in a vacuum oven at 60 °C. Similar process was used for the

fabrication of graphite/Si–P, graphite/Si, and pristine graphite electrodes, with the weight ratio of 8:1:1 for the active materials, carbon black and a polyacrylic acid (PAA) binder. CMC is a low-cost and widely used binder in commercial batteries. PAA possesses stronger adhesion than CMC and is used as a binder for electrodes with large volume change, especially for those with high mass loading [37,38]. Graphite and Si–P composite or pristine Si were mixed in the weight ratio of 85:15 before slurry fabrication for the graphite/Si–P and graphite/Si electrodes. The mass loading of Si and Si–P electrodes was 0.3–0.5 mg cm^{-2} for rate capability measurement and two different mass loadings of 0.3–0.5 mg cm^{-2} and 1–1.5 mg cm^{-2} were employed for cycling measurement. The active mass loading of the hybrid graphite/Si–P electrode was 4.5–5.2 mg cm^{-2}. All the electrodes were calendared before the cell assembly. CR2032 coin-type half cells were assembled with a Li foil as the counter electrode and 1 M LiPF$_6$ salt in ethylene carbonate (EC)/diethylene carbonate (DEC) (1:1 in volume) with 2 vol% fluoroethylene carbonate (FEC) as the electrolyte in an Ar-filled glovebox. The dosage of the electrolyte for coin cells was 200 μL. The galvanostatic charge/discharge tests were conducted in the potential window of 0.01–1.0 V on LAND cell testers at room temperature (~25 °C). Specific capacities were calculated based on the mass of active materials. The cyclic voltammetry (CV) measurements were carried out at the scanning speed of 0.1 mV s^{-1} at the potential range of 0.01–1.0 V (*vs.* Li/Li$^+$). Electrochemical impedance spectroscopy (EIS) was conducted, meanwhile the corresponding calculation of Li$^+$ diffusion coefficient (D_{Li}) was based on the following formula:

$$D=R^2T^2/(2n^4A^2F^4C^2\sigma^2) \tag{1}$$

$$Z_{re}=R_e+R_{ct}+\sigma\omega^{-1/2} \tag{2}$$

Here, R was the gas constant, T was the room temperature, n was the electron number for each molecule during Li^+ insertion, A was the area of the electrode, F was the Faraday's constant, C was molar concentration of Li^+, σ was the Warburg coefficient which had the relationship with Z_{re} and ω, where Z_{re} was the real resistance, corresponding to the X-axis in Figure 4e and ω was the angular frequency in the low frequency range in the Nyquist plots. In this experiment, the experimental conditions for the Si–P electrode and commercial Si electrode are consistent, so the Li^+ relative diffusion coefficient depends on two σ values.

3   Results and Discussion

To prove the reaction between Si and P to form chemical bonding, their reaction enthalpies were calculated. As shown in Figure 2a, the enthalpy changes of the represented reactions ($2Si+P\rightarrow Si_2P$, $Si+P\rightarrow SiP$) are negative, suggesting the reactions are thermodynamically favorable. SiP_2 would be generated near the P side and SiP would emerge near the Si side according to DFT calculation [39], which supports the possibility of formation of a Si–P core-shell structure. In our experiment, a mechanical ball-milling approach was adopted

to fabricate Si–P core-shell structures using Si particles and red P particles with a weight ratio of 5:1. The successful fabrication of Si–P composite with amorphous P surface nanolayers was verified by various characterizations. The X-ray diffraction (XRD) measurements of the starting Si, red P and the Si–P composite were conducted. Only some diffusion regions without obvious peaks existed in the XRD pattern of red P (Figure S1, Supporting Information online), indicating its amorphous structure. Characteristic peaks of Si (JCPDS 77-2110) were observed for both the Si raw materials and Si–P composite (Figure 2b). There was no new XRD peak in the XRD pattern of the Si–P composite, indicating that no new crystalline phase was produced during the mechanical ball-milling process. X-ray photoelectron spectroscopy (XPS) measurement was conducted to investigate the component of the Si–P composite and chemical bonds between Si and P. New peaks for P 2s and P 2p were observed in Si–P composite according to the XPS survey spectra of the Si raw material and Si–P composite (Figure S2), supporting the formation of P shells on the surface of Si particles by simple mechanical ball-milling [40,41]. In the high-resolution Si 2p spectrum for the pristine Si particles, the predominant peaks at 99.63 eV and 98.92 eV could be attributed to Si^0 $2p_{1/2}$ and Si^0 $2p_{3/2}$. The peaks at 103.66 eV, 103 eV, 102.46 eV and 101.23 eV corresponded to Si^{4+}, Si^{3+}, Si^{2+} and Si^{1+} [42], respectively, indicating that the surface
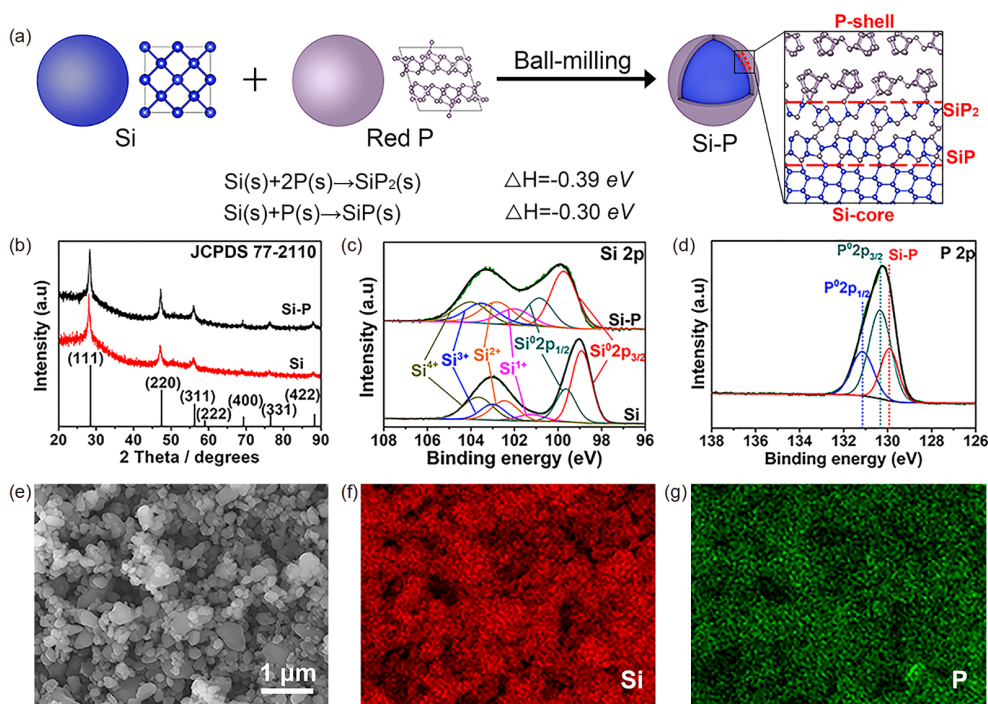

Figure 2 Fabrication and characterizations of Si–P core-shell structures. (a) Schematic of the fabrication of Si–P core-shell structures by using a ball-milling approach using Si and red P as the starting materials. During the ball-milling process, a mechanical alloying reaction takes place to form Si–P bonding. (b) XRD patterns for the pristine Si (bottom) and Si–P composite (top). (c) High-resolution Si 2p XPS spectra for the pristine Si (bottom) and Si–P composite (top). (d) High-resolution P 2p XPS spectrum for the Si–P composite. SEM image of (e) the Si–P composite and corresponding EDS mapping images of Si (f) and P (g) (color online).

layer of the pristine Si particles was slightly oxidized (Figure 2c). All the peaks in the high-resolution Si 2p spectrum for the Si–P composites shifted left, which was closely associated with the stronger electronegativity of P than that of Si [41]. In comparison to the pristine Si counterpart, the signal intensity for the oxidation of Si in the Si–P composite increased, which supported the formation of chemical bonds between Si and P. In addition, two peaks corresponding to Si $2p_{1/2}$ and Si $2p_{3/2}$ for pristine Si in the high-resolution Si 2p spectrum of the Si–P composite suggested the thin thickness of P nanolayers of the Si–P particles. The high-resolution P 2p spectrum for Si–P composite was shown in Figure 2d. The peaks at 131.13 eV and 130.33 eV could be attributed to P $2p_{1/2}$ and P $2p_{3/2}$ for pure P, respectively. The peak with lower binding energy (129.93 eV) was related to the chemical bonds between Si and P, further verifying the formation of chemical bonds between Si and P [43]. The pure P peaks exhibited more stronger intensity than the Si–P peak, suggesting the gradient of P content in the shell layer from the external surface to inner (Figure 2a, d).

Scanning electron microscopy (SEM) investigation was performed for the pristine Si and Si–P composite. The initial red P particles had very large particle size between 15 to 30 μm (Figure S3a), while the starting Si particles showed irregular morphology with much smaller particle size ranging from 200 nm–800 nm (Figure S3b). In the Si–P composite (Figure 2e), the large red P particles disappeared, and similar morphology and particle size were observed from the Si–P composite in comparison to pristine Si. The corresponding energy dispersive X-ray spectrometry (EDS) mapping result indicated the Si and P elements were uniformly distributed in the sample and there was few individual large red P particles existing in the Si–P composite, indicating the uniform dispersion and composition of Si and P (Figure 2f, g). The uniform distribution of P at the surface of

each Si particle is realized due to the bonding effects between Si and P, in good consistence with the XPS results.

High-resolution transmission electron microscopy (HRTEM) was further employed to investigate the structure and composite of the Si–P composite (Figure 3). The synthesized Si–P composite particle displayed a core-shell structure consisting of a crystalline Si core and amorphous P-containing nanoshells with thickness within 15 nm (Figure 3a). Interplanar spacing of 0.312 nm was observed in the core part of the composite particle, which is consistent with the spacing of (111) planes of crystalline Si. EDS elemental mapping under TEM was further carried out to investigate the elemental distribution in single composite particle (Figure 3d–f). A core-shell structure consisting of the Si core and P shell was confirmed for each measured composite particle. A shell structure with thickness within 15 nm was shown for each Si–P composite particle, which was uniform over an entire particle and observed in different particles. Moreover, EDS counts of P and Si signals across a particle were recorded (Figure 3b, c). The result of EDS count-position plot (Figure 3c) demonstrated an elemental P-rich surface layer with thickness within 15 nm on the surface of Si particles, which further verified the core-shell structure of the Si–P composite.

The electrochemical property of the Si–P composite was investigated in coin-cell configuration. Cyclic voltammograms (CVs) were performed in the potential range of 0.01–1 V for the initial 3 cycles and in the potential range of 0.01–2 V for the 4th cycle at 0.1 mV s^{-1}. As shown in Figure 4a, a broad peak at ~0.15 V (*vs.* Li/Li$^+$) was observed during the first-cycle cathodic scan, which was a result of the initial lithiation process of the Si–P composite. During the following cathodic scans, this peak shifted to ~0.25 V and showed a much larger peak current, indicating the enhanced electrochemical reaction kinetics after electrochemical acti-
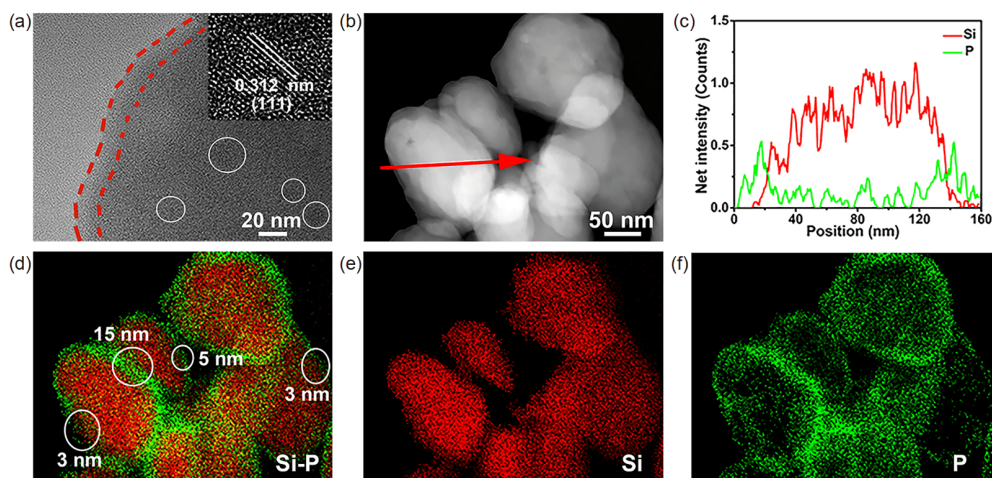

Figure 3   TEM images of the Si–P composite. (a) High-resolution TEM image of the Si–P composite. (b) Dark-field TEM image and (d–f) the corresponding EDS mapping images of Si and P for the Si–P composite. (c) EDS count-position plot across a particle in (b) (color online).

vation [44]. In the anodic scans, peaks at ~0.34 V and ~0.5 V (*vs.* Li/Li⁺) corresponded to the delithiation process of Li_xSi_y [45]. The increase in peak current after the 1st cycle also suggested enhanced delithiation kinetics. After the initial 2 cycles, the CV curves overlapped well in the potential range of 0.01–1 V (*vs.* Li/Li⁺). When the potential range was widened (0.01–2 V) in the 4th cycle, a broad peak at ~1.2 V (*vs.* Li/Li⁺) was observed during the anodic scan process. This result indicated that lithium in Li_3P produced during the first-cycle lithiation process remained stable in the potential range of 0.01–1 V (*vs.* Li/Li⁺) and would only be extracted above 1 V (*vs.* Li/Li⁺), and reversible lithiation/delithiation reactions of Si took place during electrochemical cycling between 0.01–1 V (*vs.* Li/Li⁺) for the Si–P composite. The CV curves overlapped well after the 1st cycle, indicating the good electrochemical stability of the Si–P(Li_3P) electrode. Due to the existence of Li_3P shell nanolayers with high ionic conductivity, stable electrochemical cycling with enhanced rate capability could be expected for the Si–P composite. By contrast, CV curves of pristine Si electrodes (Figure S4) showed continuous change in the intensity of peak current for the redox reactions during the measured 4 scanning cycles, indicating unstable electrochemical behaviors of the pristine Si electrode. These results highlighted the crucial

role of the P(Li_3P) nanoshell in improving the electrochemical performance of Si materials.

Galvanostatic charge/discharge measurements were conducted for the Si–P electrode at 200 mA g⁻¹ for the initial 5 cycles and the subsequent cycles were at 1,200 mA g⁻¹. The Si–P composite afforded improved electrochemical performances in comparison to the pristine Si electrode. All the initial five cycles were performed at the current density of 200 mA g⁻¹, and the subsequent cycles were conducted at the current density of 1,200 mA g⁻¹. As shown in the capacity-cycle number plot, the charge specific capacity of the Si–P electrode was 2,584 mAh g⁻¹ for the 1st cycle and 2,344 mAh g⁻¹ for the 5th cycle at 200 mA g⁻¹. Compared to the Si–P electrodes, the pristine Si electrode showed rapid capacity decay from 3,205 to 2,523 mAh g⁻¹ in 5 cycles. After 500 cycles, the charge specific capacity of the Si–P electrode was 1,178 mAh g⁻¹, much higher than 465 mAh g⁻¹ for the pristine Si electrode. The capacity retention was 71.4% from the 100th to 500th cycle for the Si–P composite. Moreover, the Si–P electrode exhibited much less polarization in comparison to the pristine Si electrode according to their voltage-capacity curves (Figure 4c, Figure S6), further suggesting improved kinetics. Battery cycling measurement at various current densities was carried out to verify the enhanced rate cap-
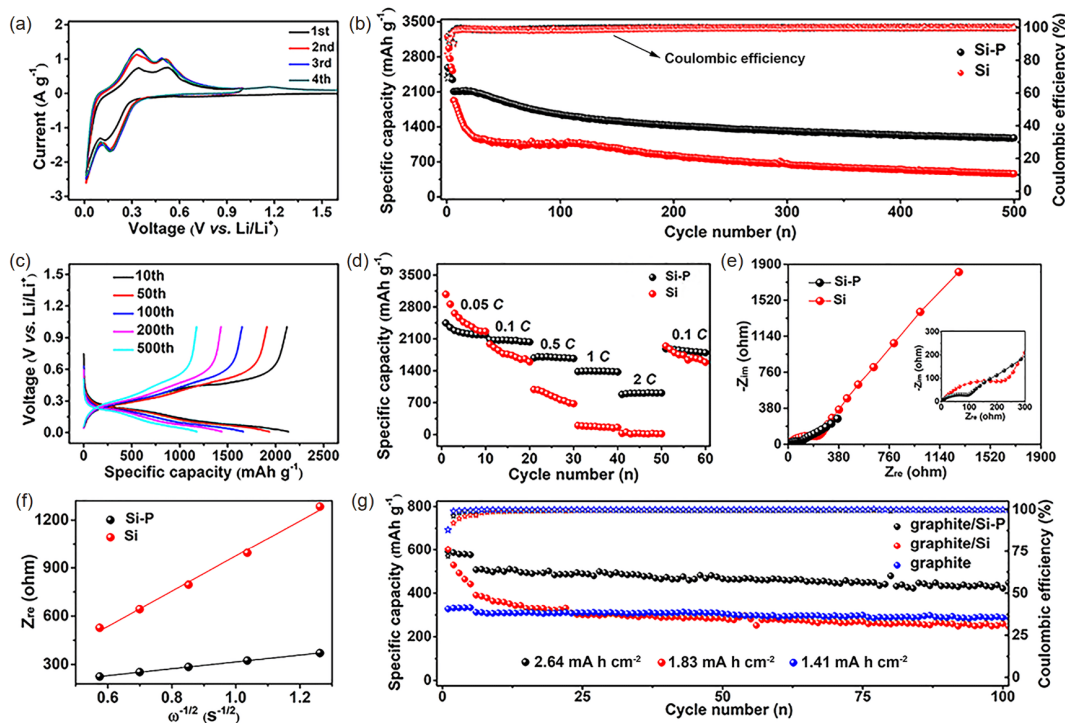

Figure 4 Electrochemical performances of the Si–P composite. (a) CV curves of the Si–P electrode at 0.1 mV s⁻¹. (b) Electrochemical cycling performances of the Si–P (black) and pristine Si (red) electrodes, and (c) the corresponding voltage-capacity profiles of the Si–P electrode. The initial five charge/discharge cycles were performed at a current density of 200 mA g⁻¹, and the subsequent cycles were conducted at a current density of 1,200 mA g⁻¹. (d) The electrochemical cycling of the pristine Si (red) and Si–P (black) electrodes at various C rates (C rate was calculated based on 4,200 mA g⁻¹). (e) Nyquist plots of the Si (red) and Si–P (black) electrodes after 50 charge/discharge cycles in the frequency range of 100 mHz–1,000 kHz. (f) Low-frequency relationships between Z_{re} and $\omega^{-1/2}$ of Si (red) and Si–P (black) electrodes after 50 charge/discharge cycles. (g) Capacity-cycle plots of graphite/Si–P, graphite/Si, and bare graphite electrodes with similar active mass loading (4.5–5.2 mg cm⁻²) cycled at 100 mA g⁻¹ after 5 activation cycles at 50 mA g⁻¹ (color online).

ability of the Si–P composite. As shown in Figure 4d, the capacity of pristine Si electrodes declined sharply and they lost almost all capacity at 1 C (158 mAh g^{-1}, C rate was based on 4,200 mA g^{-1}, the theoretical capacity of Si). On the contrary, the Si–P composite exhibited remarkable rate capability. It delivered capacities of 2,193, 2,043, 1,685, 1,383, 912 mAh g^{-1} at 0.05, 0.1, 0.5, 1, 2 C, respectively (Figure S7, C rates based on 4,200 mAh g^{-1}). When the current density returned to 0.1 C, the capacity recovered to 1,881 mAh g^{-1}, indicating the highly reversible lithiation/delithiation behavior of the Si–P electrode. The electrochemical impedance spectroscopy (EIS) results of the pristine Si electrode and the Si–P electrode after 1 and 50 cycles were shown in the Figure S8 and Figure 4e, respectively. All the Nyquist plots exhibited an irregular semicircle in the high-medium frequency region and a slant rectilinear tail in the low frequency region for the measured electrodes, where the irregular semicircle corresponded to the entire resistances and the slant rectilinear tail showed the Li ion diffusion kinetics [42]. The diameters of the semicircle of the Si–P electrodes were all clearly smaller than those of the pristine Si electrode, indicating the much more stable interfacial structure of the Si–P electrode during cycling. The rectilinear tails with larger slopes in the low frequency region suggested the faster charge transfer of the Si–P electrode than that of the pristine Si electrode, which could be attributed to the ionically conductive Li$_3$P surface layer in the Si–P electrode. The Li$^+$ diffusion coefficient (D_{Li}) of the electrodes after 50 cycles was further calculated for both electrodes, according to the equation (1) and (2) in the experimental section.

The correlation between Z_{re} and $\omega^{-1/2}$ was shown in the Figure 4f, in which the slope values (the σ values, Warburg coefficient) of the Si–P electrode and pristine Si electrode were calculated through fitting analysis as 212.2 and 1,096.7 Ω cm^2 s$^{-1/2}$, respectively. Thus, the calculated D_{Li} of the Si–P electrode was 26.7 times higher than that of the pristine Si electrode. This result further supports the enhanced electrochemical kinetics and high rate capability of the Si–P composite due to the existence of high ion-conductive Li$_3$P protective surface layers. Therefore, the P(Li$_3$P) shell in the Si–P composite stabilized the interphase of Si-based materials during electrochemical cycling, and reduced the direct contact between the active Si and liquid electrolytes. Meanwhile, high ionic conductivity of the Li$_3$P interphase layer enabled rapid lithium-ion transfer through the electrode and electrolyte interphase and thus high reversible capacity.

To explore the application of Si–P composite in high-energy-density lithium-ion batteries, 15 wt% of Si–P composite was added into graphite as the active material to fabricate a hybrid graphite/Si–P electrode during the its fabrication process. For comparison, the graphite/Si hybrid electrode with 15 wt% Si and 85 wt% graphite, and a bare graphite electrode were also fabricated using the sample electrode processing using the graphite/Si hybrid and bare graphite as the active materials, respectively. All the fabricated electrodes had similar active mass loading (4.5–5.2 mg cm^{-2}). Galvanostatic charge/discharge measurements for the graphite/Si–P, graphite/Si, and bare graphite electrodes were studied at the current density of 100 mA g^{-1} (Figure 4g). The graphite/Si–P electrode showed a high reversible capacity of 507 mAh g^{-1} after the initial 5 activation cycles, and the corresponding areal capacity reached 2.64 mAh cm^{-2}. It is noted that the graphite/Si and bare graphite electrode with similar mass loading delivered much lower areal capacities (1.83 mAh cm^{-2} for the graphite/Si hybrid electrode, 1.41 mAh cm^{-2} for the bare graphite electrode) (Figure 4g, Figure S9). For the graphite/Si–P composite electrode, the capacity contribution below 0.15 V (*vs.* Li/Li$^+$) mainly came from graphite and the capacity contribution above 0.15 V (*vs.* Li/Li$^+$) mainly arose from the Si–P composite during the lithiation process. Moreover, the graphite/Si–P electrode delivered stable cycling with 88.3% capacity retention after 100 cycles, as well as high Coulombic efficiency during cycling. For example, the Coulombic efficiency of the graphite/Si–P hybrid electrode reached a high value of 99.54% in the second cycle after activation. By contrast, the graphite/Si electrode had much worse cycling stability. Its initial capacity after activation at 100 mA g^{-1} was 391 mAh g^{-1} with a relatively low Coulombic efficiency on cycling (98.03% for the second cycle). Moreover, the graphite/Si hybrid electrode demonstrated inferior cycling stability. Its capacity decayed to 248 mAh g^{-1} after 100 cycles with capacity retention of 63.4%, which was much lower than 447 mAh g^{-1} for the graphite/Si–P composite and even lower than 291 mAh g^{-1} for bare graphite. The improved electrochemical performance of the graphite/Si–P hybrid electrode indicates the successful design of ionically conductive and stable P(Li$_3$P) interphase on Si for improving high capacity anodes, suggesting the promise of using Si–P composite in next-generation high-performance lithium-ion batteries.

The morphology and the structure of the Si–P composite after cycling have been investigated using TEM, EDS mapping, and SEM to further support its enhanced electrochemical performance. Figure 5a showed the TEM image of Si–P composite, which showed the intact particle structure. Meanwhile, the SAED pattern collected at the edge of a particle (the inset of Figure 5a) displayed three halo-like rings with some well-distributed spots attributed to (101), (103) and (202) planes of crystalline Li$_3$P [46]. These results verified the formation of the Li$_3$P after the first charge/discharge cycle and the stable structure of the Si–P composite. Moreover, ultrathin nanodomains with clear lattice fringes of 0.186 nm for (112) plane of Li$_3$P were densely distributed on the surface of the Si–P(Li$_3$P) observed under HRTEM (Figure S10), again indicating the irreversible conversion of P nanoshells to Li$_3$P nanoshells on active Si materials. As
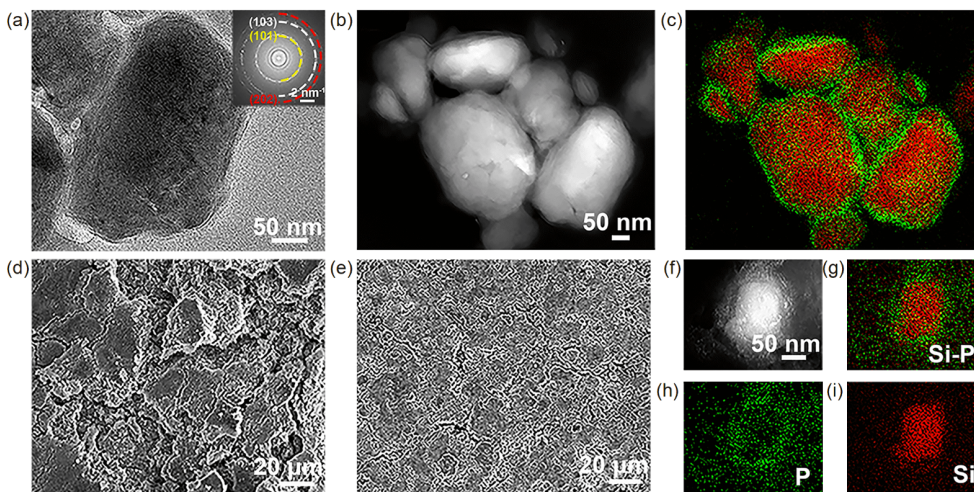
Figure 5 Characterizations of Si–P and pristine Si after cycling. (a) TEM image of the Si–P composite after 1st charge/discharge cycle. (b) Dark-field TEM image and (c) the elemental mapping images of the Si–P composite after 1 discharge/charge cycle. SEM images of (d) the Si electrode and (e) the Si–P electrode after 50 charge/discharge cycles. (f) Dark-field TEM image and (g–i) elemental mapping images of the Si–P composite after 50 charge/discharge cycles (color online).

revealed by the dark-field TEM and the corresponding Si and P elemental mapping images (Figure 5b, c), the core-shell structure of the Si–P (Li$_3$P) material remained unchanged after a full charge/discharge cycle, indicating the good stability of the Si–P composite at the single-particle level. Moreover, the Si–P electrode remained intact without fracture compared with Si electrodes after 1 full discharge/charge cycle, indicating the good stability of the Si–P composite at the electrode level (Figure S11). The cross-section SEM images have been provided for Si–P electrodes before and after 20 charge/discharge cycles at 1,200 mA g^{-1} (Figure S12). The thickness of the measured electrode increased from 20 μm to 25 μm after cycling. Figure 5d, e displayed the SEM images of the Si and Si–P electrode after 50 charge/discharge cycles. The Si–P electrode maintained the intact surface structure without facture while the pristine Si electrode was severely damaged after 50 cycles, due to the severe strain caused by accumulation of large amounts of SEI during cycling. The dark-field TEM and the corresponding Si, P elemental mapping images of Si–P composite after 50 cycles were shown in Figure 5f–i. The core-shell structure of the Si–P(Li$_3$P) was well maintained after 50 cycles, suggesting the good stability of the protection layer. Not only did the intact Li$_3$P layer stabilize the interface to maintain the integrity of the surface of the Si–P electrode, but also it provided high ionic conductivity, which is verified from the above electrochemical results including enhanced cycling stability and rate capabilities. We further investigated the morphology and structure of the Si–P electrode after 500 cycles (Figure S13). Overall, the Si–P electrode remained intact without damage, which reduced/avoided the direct contact between the liquid electrolyte and active Si and suppressed undesired side reactions. By contrast, the struc-

ture of the pristine Si electrode collapsed after long cycling due to the accumulation of thick SEI layers and volume change during lithiation/delithiation process. Therefore, the Li$_3$P layer of the Si–P(Li$_3$P) significantly reduced the side reactions between the electrolyte and active Si, and the accumulation of SEI, and thus improved the stability and cycling performances of the electrode. Also, the resistance of the electrolyte was significantly reduced and the rate capability of the electrode was greatly improved due to the existence of ionically conductive Li$_3$P surface protective layers.

4   Conclusions

A Si–P composite featuring a Si core with a ultrathin P nanoshell (within 15 nm) was fabricated through a simple one-step mechanical ball-milling approach using red P and Si waste from photovoltaic industry. The P nanoshell was chemically bonded to a Si core, which converted to an ionically conductive Li$_3$P surface protective nanolayer irreversibly for Si in the cutoff voltage range of 0.01–1 V (*vs.* Li/Li$^+$). The as-generated Li$_3$P nanolayer on Si reduced the direct contact between active Si and liquid electrolytes, resisted the excessive consumption of the electrolyte and active Li, and inhibited the continuous growth of SEI layers, and thus prolonged the electrochemical cycle life. Moreover, the ionically conductive Li$_3$P nanoshell enabled fast ion transfer at the Si surface, which led to much improved rate capability. As expected, a Si–P electrode showed high reversible capacity (1,178 mAh g^{-1} after 500 cycles at 1,200 mA g^{-1}) and excellent rate capability (912 mAh g^{-1} at 2 C). With 15 wt% addition to commercial graphite, a graphite/Si–P hybrid electrode exhibited a high specific capa-

city of 507 mAh g^{-1} at a high areal capacity of 2.64 mAh cm^{-2}, which was much higher than 312 mAh g^{-1} and 1.41 mAh cm^{-2} for the bare graphite electrode, and 391 mAh g^{-1} and 1.83 mAh cm^{-2} for the graphite/Si hybrid electrode with a similar active mass loading between 4.5–5.2 mg cm^{-2} at 100 mA g^{-1}. Moreover, the graphite/Si–P composite exhibited superior cycle retention of 88.3% after 100 cycles.

Conflict of interest   The authors declare no conflict of interest.

Supporting information   The supporting information is available online at http://chem.scichina.com and http://link.springer.com/journal/11426. The supporting materials are published as submitted, without typesetting or editing. The responsibility for scientific accuracy and content remains entirely with the authors.

1   Cano ZP, Banham D, Ye S, Hintennach A, Lu J, Fowler M, Chen Z. *Nat Energy*, 2018, 3: 279–289
2   Choi JW, Aurbach D. *Nat Rev Mater*, 2016, 1: 16013
3   Jin Y, Zhu B, Lu Z, Liu N, Zhu J. *Adv Energy Mater*, 2017, 7: 1700715
4   Li JY, Xu Q, Li G, Yin YX, Wan LJ, Guo YG. *Mater Chem Front*, 2017, 1: 1691–1708
5   Luo W, Chen X, Xia Y, Chen M, Wang L, Wang Q, Li W, Yang J. *Adv Energy Mater*, 2017, 7: 1701083
6   Sun Y, Liu N, Cui Y. *Nat Energy*, 2016, 1: 16071
7   Liu Y, Zhou G, Liu K, Cui Y. *Acc Chem Res*, 2017, 50: 2895–2905
8   Wang J, Liao L, Lee HR, Shi F, Huang W, Zhao J, Pei A, Tang J, Zheng X, Chen W, Cui Y. *Nano Energy*, 2019, 61: 404–410
9   Zeng Z, Liu N, Zeng Q, Lee SW, Mao WL, Cui Y. *Nano Energy*, 2016, 22: 105–110
10 Huang W, Attia PM, Wang H, Renfrew SE, Jin N, Das S, Zhang Z, Boyle DT, Li Y, Bazant MZ, McCloskey BD, Chueh WC, Cui Y. *Nano Lett*, 2019, 19: 5140–5148
11 Huang W, Wang J, Braun MR, Zhang Z, Li Y, Boyle DT, McIntyre PC, Cui Y. *Matter*, 2019, 1: 1232–1245
12 Ko M, Chae S, Cho J. *ChemElectroChem*, 2015, 2: 1645–1651
13 Wu H, Cui Y. *Nano Today*, 2012, 7: 414–429
14 Schiele A, Breitung B, Hatsukade T, Berkes BB, Hartmann P, Janek J, Brezesinski T. *ACS Energy Lett*, 2017, 2: 2228–2233
15 Schiele A, Breitung B, Mazilkin A, Schweidler S, Janek J, Gumbel S, Fleischmann S, Burakowska-Meise E, Sommer H, Brezesinski T. *ACS Omega*, 2018, 3: 16706–16713
16 Jin Y, Li S, Kushima A, Zheng X, Sun Y, Xie J, Sun J, Xue W, Zhou G, Wu J, Shi F, Zhang R, Zhu Z, So K, Cui Y, Li J. *Energy Environ Sci*, 2017, 10: 580–592
17 Ko M, Chae S, Ma J, Kim N, Lee HW, Cui Y, Cho J. *Nat Energy*, 2016, 1: 16113
18 Meng Q, Li G, Yue J, Xu Q, Yin YX, Guo YG. *ACS Appl Mater Interfaces*, 2019, 11: 32062–32068
19 Wang J, Liao L, Li Y, Zhao J, Shi F, Yan K, Pei A, Chen G, Li G, Lu Z, Cui Y. *Nano Lett*, 2018, 18: 7060–7065
20 Chen T, Wu J, Zhang Q, Su X. *J Power Sources*, 2017, 363: 126–144
21 Li G, Huang LB, Yan MY, Li JY, Jiang KC, Yin YX, Xin S, Xu Q, Guo YG. *Nano Energy*, 2020, 74: 104890
22 Men X, Wang T, Xu B, Kong Z, Liu X, Fu A, Li Y, Guo P, Guo YG, Li H, Zhao XS. *Electrochim Acta*, 2019, 324: 134850
23 Xue L, Xu G, Li Y, Li S, Fu K, Shi Q, Zhang X. *ACS Appl Mater Interfaces*, 2013, 5: 21–25
24 Guo S, Hu X, Hou Y, Wen Z. *ACS Appl Mater Interfaces*, 2017, 9: 42084–42092
25 Liu N, Wu H, McDowell MT, Yao Y, Wang C, Cui Y. *Nano Lett*, 2012, 12: 3315–3321
26 Liu N, Lu Z, Zhao J, McDowell MT, Lee HW, Zhao W, Cui Y. *Nat Nanotech*, 2014, 9: 187–192
27 Xu Q, Li JY, Sun JK, Yin YX, Wan LJ, Guo YG. *Adv Energy Mater*, 2017, 7: 1601481
28 Li Y, Yan K, Lee HW, Lu Z, Liu N, Cui Y. *Nat Energy*, 2016, 1: 15029
29 Sun Y, Lopez J, Lee HW, Liu N, Zheng G, Wu CL, Sun J, Liu W, Chung JW, Bao Z, Cui Y. *Adv Mater*, 2016, 28: 2455–2461
30 Chen J, Fan X, Li Q, Yang H, Khoshi MR, Xu Y, Hwang S, Chen L, Ji X, Yang C, He H, Wang C, Garfunkel E, Su D, Borodin O, Wang C. *Nat Energy*, 2020, 5: 386–397
31 Etacheri V, Haik O, Goffer Y, Roberts GA, Stefan IC, Fasching R, Aurbach D. *Langmuir*, 2012, 28: 965–976
32 Qudoos A, Jeon IK, Kim SS, Lee JB, Kim HG. *Materials*, 2020, 13: 251
33 Ding Y, Li ZF, Timofeeva EV, Segre CU. *Adv Energy Mater*, 2018, 8: 1702134
34 Reinhold R, Stoeck U, Grafe HJ, Mikhailova D, Jaumann T, Oswald S, Kaskel S, Giebeler L. *ACS Appl Mater Interfaces*, 2018, 10: 7096–7106
35 Pralong V, Souza DCS, Leung KT, Nazar LF. *Electrochem Commun*, 2002, 4: 516–520
36 Chen F, Cheng S, Liu J, Li S, Ouyang W, Yuan K, Liu B. *J Power Sources*, 2020, 477: 228744
37 Wu J, Zhang Q, Liu S, Long J, Wu Z, Zhang W, Pang WK, Sencadas V, Song R, Song W, Mao J, Guo Z. *Nano Energy*, 2020, 77: 105118
38 Liu Y, Tai Z, Zhou T, Sencadas V, Zhang J, Zhang L, Konstantinov K, Guo Z, Liu HK. *Adv Mater*, 2017, 29: 1703028
39 Kohn W, Sham LJ. *Phys Rev*, 1965, 140: A1133–A1138
40 Li C, Wang S, Zhang X, Jia N, Yu T, Zhu M, Liu D, Tao X. *CrystEngComm*, 2017, 19: 6986–6991
41 Swain BP, Hwang NM. *Appl Surf Sci*, 2008, 254: 5319–5322
42 Zheng G, Xiang Y, Xu L, Luo H, Wang B, Liu Y, Han X, Zhao W, Chen S, Chen H, Zhang Q, Zhu T, Yang Y. *Adv Energy Mater*, 2018, 8: 1801718
43 Park BH, Haghighat-Shishavan S, Nazarian-Samani M, Kim KB. *J Power Sources*, 2019, 434: 226759
44 Zhu Y, Wen Y, Fan X, Gao T, Han F, Luo C, Liou SC, Wang C. *ACS Nano*, 2015, 9: 3254–3264
45 Park BH, Jeong JH, Lee GW, Kim YH, Roh KC, Kim KB. *J Power Sources*, 2018, 394: 94–101
46 Zheng Z, Wu HH, Liu H, Zhang Q, He X, Yu S, Petrova V, Feng J, Kostecki R, Liu P, Peng DL, Liu M, Wang MS. *ACS Nano*, 2020, 14: 9545–9561